Yupeng Cao[1]
Shanghai Nuclear Engineering Research and Design Institute,
Department of Component Research and Design,
Shanghai 200233, China
e-mail: caoyupeng@snerdi.com.cn

Guian Qian[1]
Laboratory for Nuclear Materials,
Paul Scherrer Institute,
Villigen 5232, Switzerland;
State Key Laboratory for Nonlinear Mechanics (LNM),
Institute of Mechanics,
Chinese Academy of Sciences,
Beijing 100190, China
e-mail: guian.qian@psi.ch

Yinbiao He
Department of Component Research and Design,
Shanghai Nuclear Engineering Research and Design Institute,
Shanghai 200233, China

Markus Niffenegger
Laboratory for Nuclear Materials,
Paul Scherrer Institute,
Villigen 5232, Switzerland

Yuh J. Chao
Department of Mechanical Engineering,
University of South Carolina,
Columbia, SC 29208

Constraint Assessment for Specimens Tested Under Uniaxial and Biaxial Loading Conditions

In structural integrity analysis of reactor pressure vessels (RPVs), a postulated shallow crack is subjected to biaxial far-field stresses. However, the fracture toughness K_c or J_c, which is an important material property for the structural integrity assessment of RPVs, is usually obtained from testing deeply cracked compact tension (C(T)) or single-edged bending (SE(B)) specimens under uniaxial loading. Thus, the fracture toughness data do not reflect the biaxial loading state that cracks in a RPV are subjected to. Cruciform bending specimen was therefore developed to simulate the biaxial stress state. In this paper, a series of finite element (FE) simulations of the cruciform specimens containing different crack geometries and of different material properties are conducted. The crack tip stress fields are analyzed, and the constraint is investigated using the J–A_2 theory. The results show that the biaxial effect is material property dependent which could be useful for the optimization of the test method and the better design of cruciform specimens. The trends about the biaxial loading effect revealed in this study would also be helpful in estimating the safe operating life of RPVs. [DOI: 10.1115/1.4039346]

Introduction

Generally, cracks detected during in-service inspections of reactor pressure vessels (RPVs) in nuclear power plants are shallow cracks. The crack in RPV is subjected to combined thermal–mechanical loads, such as normal operational pressure temperature (P–T) transients and pressurized thermal shock (PTS) transients. The thermal, pressure, and residual stresses in the RPV wall are combined to form a biaxial stress state at the crack tip as schematically shown in Fig. 1, where t is the thickness of the RPV wall. However, the fracture toughness of materials, K_c or J_c, required for the structural integrity assessment of the RPV is typically obtained from the conventional deeply cracked single-edged bending (SE(B)) and/or compact tension (C(T))specimens tested under uniaxial loading. The crack-tip stress state in test specimens (uniaxial) could be quite different from that of a real crack in RPV (biaxial).

The cruciform bending specimen (CR(B)) specimen is a specially designed specimen which can introduce an in-plane and out-of-plane bending stress field that approximates the biaxial stress state resulted from P–T or PTS loading. The biaxial loading ratio in a CR(B) specimen can be adjusted by the appropriate span width ratios of the longitudinal beam arm to the transverse one. The CR(B) specimen can thus be used to address the influence of biaxial stress on the crack-tip constraints, thereby providing clues for predicting the potential fracture of RPVs.

A series of large ($100 \times 100\,\text{mm}^2$ cross section) cruciform specimen made of A533B steel were tested by Bass et al. [1]. Joyce et al. [2] developed a medium scale CR(B) specimens ($50 \times 50\,\text{mm}^2$ cross section) made of the same steel. More recently, Hohe et al. [3] showed that the biaxial effects observed on large-scale CR(B) specimen could be reproduced in the small-scale CR(B) specimen ($10 \times 20\,\text{mm}^2$ cross section). Joyce et al.

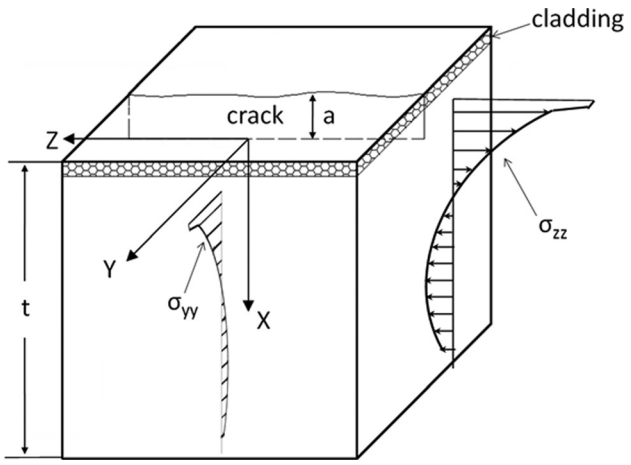

Fig. 1 Biaxial stress state of the crack in RPV wall under PTS transients

[1]Corresponding authors.

Contributed by the Pressure Vessel and Piping Division of ASME for publication in the Journal of Pressure Vessel Technology. Manuscript received August 13, 2017; final manuscript received January 30, 2018; published online April 3, 2018. Assoc. Editor: David L. Rudland.

[4] summarized the database of several RPV materials tested with both biaxial- and uniaxial-loaded specimens to study the effect of biaxial loading on the master curve transition temperature. Numerical studies on CR(B) were conducted recently by Sharp and Chao [5,6]. They showed that the biaxial effect as seen from the tests can be predicted by the J–A_2 theory. These investigations, however, were not conclusive to demonstrate that biaxial loading imposed through the use of a CR(B) specimen geometry has any pronounced effect on the fracture toughness. Joyce and coworkers pointed out that the detailed stress analysis should be used to characterize the constraints when biaxial effect on the fracture toughness would become significant [4].

This study focuses on evolution of any potential biaxial effect in the CR(B) specimens with various material tensile properties and the crack depths. The range of tensile properties considered reflects the increase in the yield strength with the decrease in hardening exponent of RPV steels due to irradiation and temperature. Different crack depths ($a/W = 0.08$ and 0.15) are considered to study the influence of crack depth on the biaxial loading effects. The constraint effect along the three-dimensional crack front is characterized with the J–A_2 methodology, in which J is used as the applied load and A_2 as the constraint level. Comparison with SE(B) specimen was also made.

J–A_2 Methodology

The uniaxial tensile property of the material represented by the Ramberg–Osgood stress–strain relationship has the form

$$\frac{\varepsilon}{\varepsilon_0} = \frac{\sigma}{\sigma_0} + \alpha\left(\frac{\sigma}{\sigma_0}\right)^n \tag{1}$$

where σ_0 and $\varepsilon_0 = \sigma_0/E$ can be taken as the yield stress and the yield strain, respectively; E is the Young's modulus, α is a material constant, and n is the strain hardening exponent.

The stress fields at a crack tip in a power-law plasticity material such as the Ramberg–Osgood material in Eq.(1) may be characterized by the classical HRR solution (after Hutchinson and Rice and Rosengren) [7–9] from fracture mechanics theory as

$$\sigma_{ij} = \sigma_0\left(\frac{J}{\alpha\varepsilon_0\sigma_0 I_n r}\right)^{1/n+1}\tilde{\sigma}_{ij}(\theta, n) \tag{2}$$

where I_n is an integration constant that depends on n; i and j represent r and θ in a polar coordinate system with origin at the crack tip, and $\tilde{\sigma}_{ij}(\theta, n)$ is the dimensionless stress function of n and θ.

It is well known that the HRR solution can be used to characterize the stress fields only under small-scale yielding condition and high constraint specimen geometry such as the deeply cracked C(T) and SE(B) specimens according to the ASTM test standard [10]. The crack tip stresses in the low constraint geometry generally deviate from the HRR solution gradually as the load increases. In order to solve this problem, Yang et al. [11,12] and Chao et al. [13] developed the asymptotic solutions near a crack tip, which includes several higher-order terms. It was demonstrated that the stress, strain, and displacement fields in either high or low constraint specimen geometry can be well characterized by the analytical solution with only three terms, which can be written as

$$\frac{\sigma_{ij}}{\sigma_0} = A_1\left[\left(\frac{r}{L}\right)^{s_1}\tilde{\sigma}_{ij}^{(1)}(\theta,n) + A_2\left(\frac{r}{L}\right)^{s_2}\tilde{\sigma}_{ij}^{(2)}(\theta,n) + A_2^2\left(\frac{r}{L}\right)^{s_3}\tilde{\sigma}_{ij}^{(3)}(\theta,n)\right] \tag{3}$$

where the angular functions $\tilde{\sigma}_{ij}^{(k)}(\theta, n)$ $(k = 1, 2, 3)$ are the dimensionless functions of n and θ, the stress power exponents s_1, s_2, s_3 $(s_1 < s_2 < s_3)$ are only dependent of the hardening exponent n, $s_1 = -(1/(n+1))$ and $s_3 = 2s_2 - s_1$ for $n > 3$. L is a characteristic length parameter which can be chosen as the crack length a, specimen thickness W, or a unit length (e.g., 1 mm). The parameters A_1 is given by

$$A_1 = \left(\frac{J}{\alpha\varepsilon_0\sigma_0 I_n L}\right)^{-s_1} \tag{4}$$

A_2 is an undetermined parameter and is a function of the geometry of the specimen and the loading. Hence, A_2 can be used as a quantitative measure of the constraint effect. The numerical values of the parameters $\tilde{\sigma}_{ij}^{(k)}(\theta, n)$, I_n and S_k in Eqs. (3) and (4) have been tabulated by Chao and Zhang [14].

For convenience, the parameters required for the application of the J–A_2 theory were fitted by Wang et al. [15]. The stress power exponents s_2 and s_3 are

$$\begin{cases} s_2(n) = -0.888e^{-0.7803n} + 0.0725 & (3 \le n \le 9) \\ s_2(n) = 0.079e^{-0.0372n} + 0.0152 & (9 \le n \le 50) \end{cases} \tag{5}$$

$$s_3(n) = 2s_2(n) - s_1(n) \quad (3 \le n \le 50) \tag{6}$$

The equations for the angular functions $\tilde{\sigma}_{ij}^{(k)}(\theta, n)$ at $\theta = 0$ and the integration constant I_n are fitted as follows:

$$\tilde{\sigma}_{\theta\theta}^{(1)}(\theta = 0, n) = -1.217e^{-0.3867n} - 0.640e^{-0.0680n} + 2.8473 \quad (3 \le n \le 50) \tag{7}$$

$$\begin{cases} \tilde{\sigma}_{\theta\theta}^{(2)}(\theta = 0, n) = -0.04270 + 0.2117n - 0.04659n^2 \\ \qquad\qquad + 0.004605n^3 - 0.0001729n^4 \quad (3 \le n \le 8) \\ \tilde{\sigma}_{\theta\theta}^{(2)}(\theta = 0, n) = 0.14361e^{-0.03147n} + 0.20774 \quad (8 \le n \le 50) \end{cases} \tag{8}$$

$$\tilde{\sigma}_{\theta\theta}^{(3)}(\theta = 0, n) = 10.45624e^{-0.33465n} - 17.9685e^{0.013078n} + 13.78619 \quad (3 \le n \le 50) \tag{9}$$

$$I_n = 1.11366e^{-0.0625n} + 2.16658e^{-0.3900n} + 3.91467 \tag{10}$$

In this study, the J–A_2 method is used to characterize the crack-tip constraints of both the CR(B) and SE(B) specimens containing shallow cracks with different material properties.

Finite Element Modeling

Fracture toughness tests using a large-scale CR(B) specimen can be very expensive. In the case of limited material availability, for example, the RPV surveillance materials and the heat-affected zone materials, a large specimen cannot be cut from the component and thus a small-scale specimen is desirable. Moreover, a small CR(B) specimen has the width and thickness similar to the conventional standard-sized specimen for elastic–plastic fracture toughness testing [3], which can somewhat remove the size effect in studying of biaxial loading effect. Therefore, the finite element (FE) analyses in this study adopted the small CR(B) with different crack depths combined with a series of tensile properties.

Considering that a large test matrix of CR(B) specimens were developed by Hohe et al. [3], the small CR(B) specimens tested by them are modeled in this study, as shown in Fig. 2. In order to perform a comparison, the SE(B) specimens with the same cross section and crack depths as those of the CR(B) specimen (see Fig. 3) are also analyzed. The through-wall cracks with straight front are modeled. The dimensions of the specimens are listed in Table 1. In the numerical calculation, the CR(B) specimen model is loaded by the central support with the prescribed displacement and the four rollers are fixed to ensure the equal spans as indicted

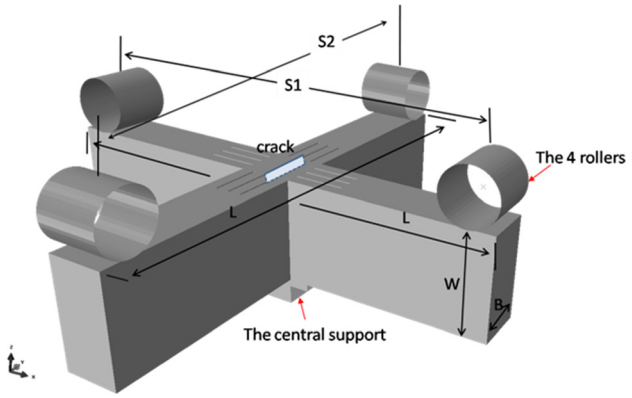

Fig. 2 Geometry of the CR(B) specimen

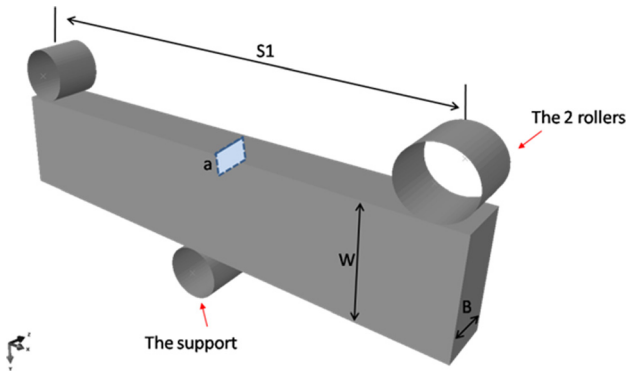

Fig. 3 Geometry of the SE(B) specimen

Table 1 Sizes of specimens

Specimen type	B (mm)	W (mm)	S_1 (mm)	S_2 (mm)	L (mm)	a_0/W
CR(B)	10	20	80	80	90	0.08, 0.15
SE(B)	10	20	80	/	90	0.08, 0.15

Table 2 The assumed Ramberg–Osgood parameters of the RPV materials

Material IDs	E/σ_0	α	E (MPa)	n
1	800	1.6	206,000	5
2	500	1	206,000	10
3	300	0.6	206,000	20

in Fig. 2. The SE(B) specimen model is also loaded by the prescribed displacement of the support as shown in Fig. 3, where S_1 and S_2 are the spans, W is the width, a is the crack depth, and B is the thickness of the specimen. The support and the rollers are modeled as the rigid bodies.

Three sets of the Ramberg–Osgood parameters (see Table 2 and Fig. 4) are considered to assess the influence of material tensile properties on the biaxial loading. The Poisson's ratio ν is assumed as 0.3. These ranges of tensile properties reflect the increase in the yield strength with the decrease in hardening exponent that are the characteristics of RPV steels due to irradiation and the variations in the stress–strain relationship with temperature.

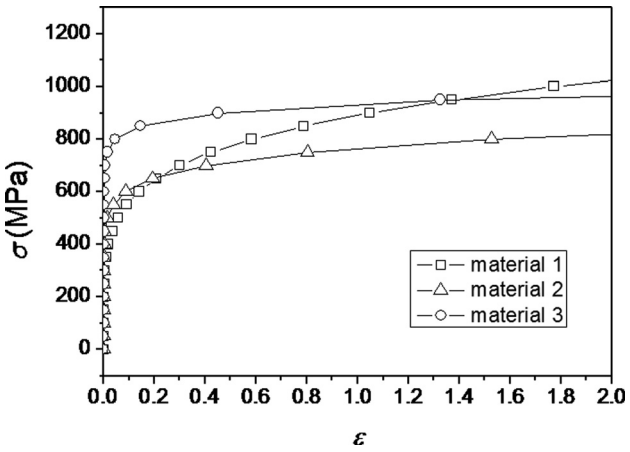

Fig. 4 The stress–strain curves

By taking into account of symmetry, only one-quarter of the CR(B) and SE(B) specimens are modeled using the commercial FE code ABAQUS [16] as shown in Fig. 5. For each type of the specimen, two straight crack depths ($a_0/W = 0.08$, $a_0/W = 0.15$) are considered. The support and the rollers interact with the deformable test specimen via the frictionless contact formulation. The minimum element size along the ligament ahead of the crack tip is 10 μm. In the range of 0.5 mm around the crack tip, the FE mesh designs are similar in all the models. The elements used are the reduced-integration linear elements (designated as C3D8R in ABAQUS). A coordinate system for the specimens are shown in Fig. 5 such that the x-axis lies in the crack plane and is normal to the straight crack front; y-axis is orthogonal to the crack plane, and the z-axis lies in the thickness direction. The origin of the coordinate system is located at the crack tip in the center plane.

Constraint Analysis With J–A_2 Method

The constraint parameter A_2 in Eq. (3) is determined using a point match technique described as following:

(1) Obtain the opening stress distribution $\sigma_{\theta\theta}$ (σ_{yy} in this study as shown in Fig. 5) at a point of interest along the crack front (Z axis in Fig. 5) from the FE analysis.
(2) Set the $\sigma_{\theta\theta}$ from the FE analysis equal to the three-term analytical function Eq. (3) to create a quadratic equation with respect to A_2. The characteristic length parameter L is set to be 1 mm.
(3) Solve the quadratic equation for A_2 at each node along the ligament (in the positive direction of X axis in Fig. 5).

A_2 values are plotted in Figs. 6 and 7 to quantify the constraints. Similar to T-stress and Q-stress theories, the higher A_2 means the higher constraint, which is closer to the HRR solutions. Specifically, the $\sigma_{\theta\theta}$ values in the range of $r/(J/\sigma_0) = 2$–5, $\theta = 0$ deg are used to determine an average A_2 in this paper.

Figures 6(*a*)–6(*c*) show the distributions of A_2 for CR(B) and SE(B) specimens with $a_0/W = 0.15$ under different loading levels (J-integrals). The A_2 results are plotted from the center to the crack ends of the specimen, with $x/(B/2) = 0$ denoting specimen center and $x/(B/2) = 1$ representing ends of the crack front. The same values of J at the center plane are chosen for all cases to facilitate the comparison.

It is seen in Fig. 6(*c*) that the SE(B) specimen with $E/\sigma_0 = 300$ shows the highest A_2 (approximately -0.265) at the center plane. It should be mentioned that since only the shallow cracks are considered in this paper, all the crack tips have constraint loss and thus show negative A_2. For the SE(B) specimen, A_2 decreases from specimen center to the crack ends, i.e., with increasing $x/(B/2)$. A_2 decreases drastically in the region close to the crack ends, especially for the SE(B) specimen with $E/\sigma_0 = 800$

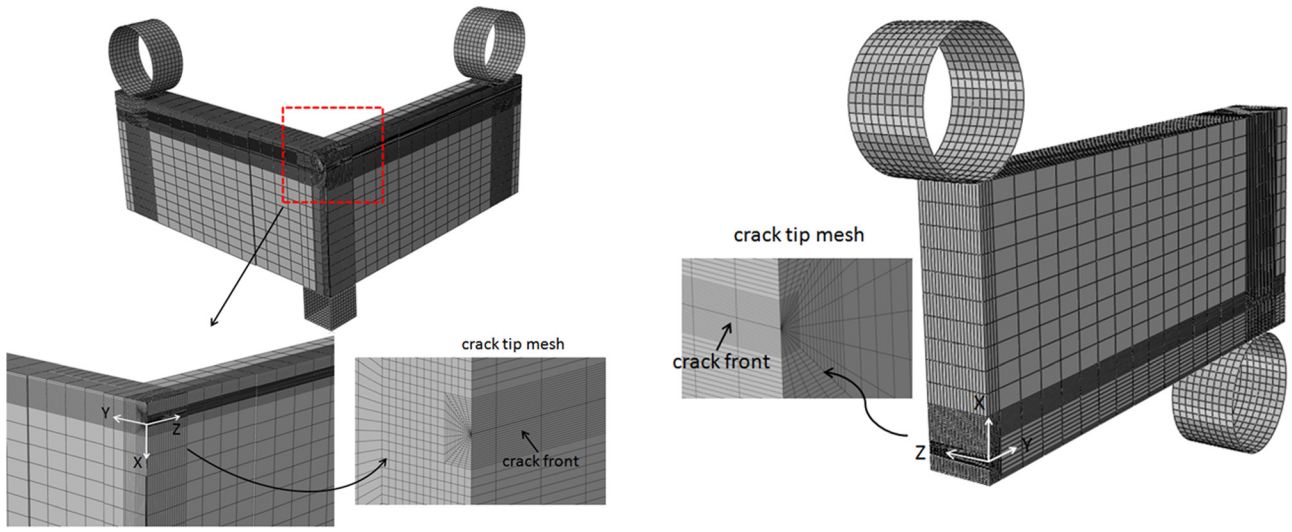

(*a*) (*b*)

Fig. 5 Finite element meshes for (*a*) the CR(B) and (*b*) SE(B) specimens

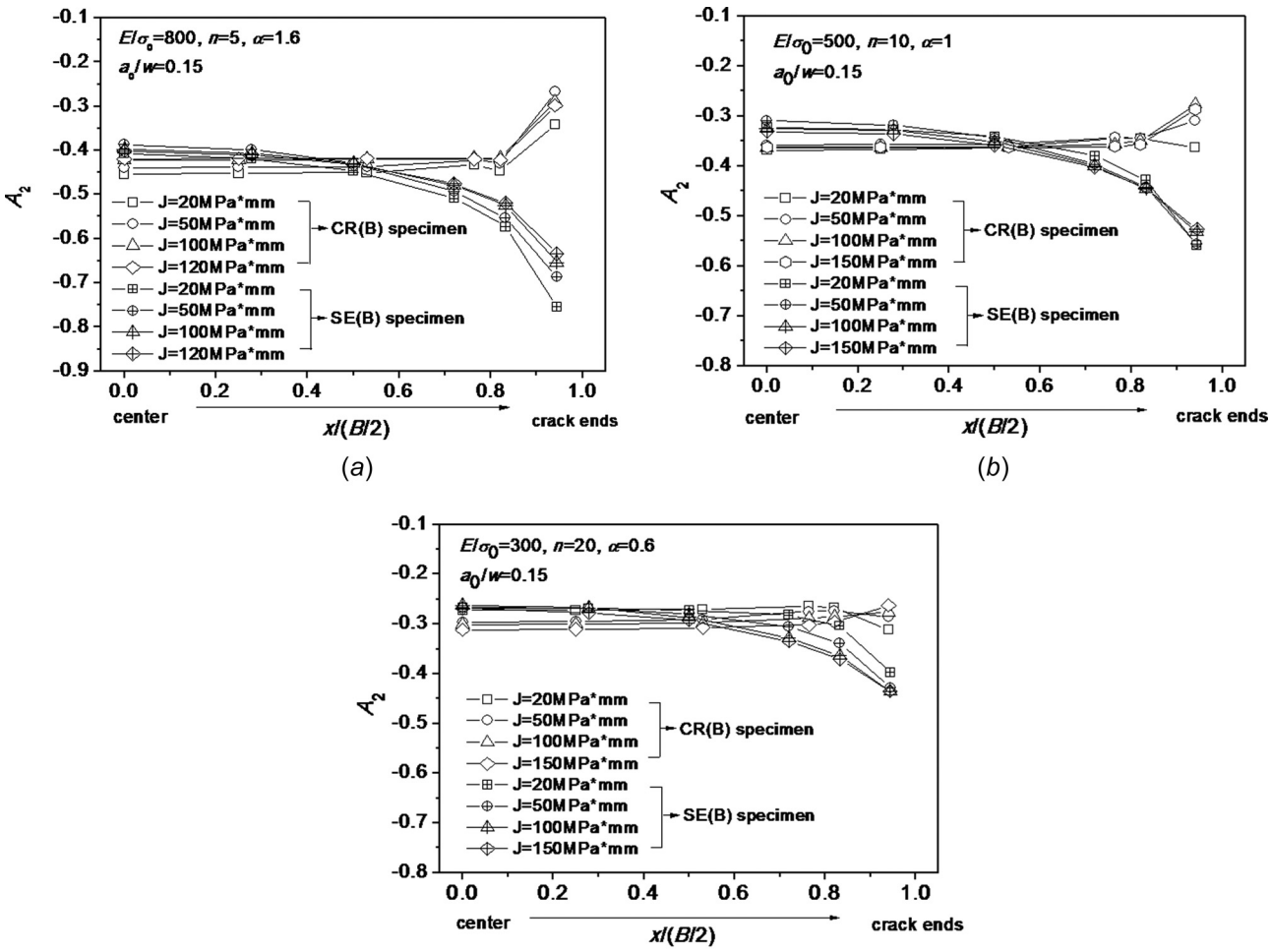

(*a*) (*b*) (*c*)

Fig. 6 Variation of A_2 across the thickness with crack depth $a_0/W = 0.15$ for: (*a*) material 1 ($E/\sigma_0 = 800$, $n = 5$, $\alpha = 1.6$), (*b*) material 2 ($E/\sigma_0 = 500$, $n = 10$, $\alpha = 1$), and (*c*) material 3 ($E/\sigma_0 = 300$, $n = 20$, $\alpha = 0.6$)

and 500 in Figs. 6(*a*) and 6(*b*). With the increase of E/σ_0, the values of A_2 for the SE(B) specimen become more negative near the crack ends. For the material with $E/\sigma_0 = 800$, A_2 for the SE(B) specimen drops to a low value of -0.729, while the value is -0.483 at the center plane as shown in Fig. 6(*a*). In contrast, for the CR(B) specimen, regardless of the materials, A_2 keeps almost constant along most part of the crack front, and even increases near the ends of the crack front $x/(B/2) = 1$. In other words, the CR(B) specimen shows no constraint transition from plane strain condition in the interior of the specimen to plane stress condition at the ends of the crack front, which is different from the SE(B) specimen. This phenomenon is also observed in the tests of Hohe et al. with the German RPV steel (22NiCrMo37) [3]. In their study, the increase of the fatigue crack depth at the ends of the crack was observed on the fracture surface of the CR(B) specimens, which is in contrast to the SE(B) specimen. In addition, an even distribution of the cleavage initiation spots through the CR(B) specimen thickness was observed, whereas the initiation sites for the SE(B) specimens were found at locations away from the free surfaces.

Figures 6(*a*)–6(*c*) also compare the influence of material properties on the crack-tip constraint for the SE(B) and CR(B) specimens. It is observed that for the three investigated materials, constraints of the SE(B) specimen are slightly higher than those of the CR(B) specimen in the region near the center plane. The material with $E/\sigma_0 = 800$ has the largest difference of A_2 between the CR(B) and the SE(B) specimens especially near the position of $x/(B/2)=1$. The least effect of biaxial loading is observed for the material with $E/\sigma_0 = 300$. This comparison indicates that the biaxial effect is material dependent and more pronounced in the material with lower yield stress.

The distributions of J along the crack front for the SE(B) and CR(B) specimens are shown in Figs. 8(*a*)–8(*c*). The J values at each crack front location are normalized by J at the midplane. For the SE(B) specimen, J peaks at the midplane and decreases toward the free surface. As the load increases, the difference of J at the midplane and at the region near the free surface becomes pronounced. Increased E/σ_0 promotes a slightly more uniform front distribution of J. For CR(B) specimen, the maximum J occurs at the crack end and the distributions of J are nearly uniform along most part of the crack front at each loading level.

In order to assess the influence of crack depth on the crack-tip constraint, specimens with a shallower crack ($a_0/W = 0.08$) are also analyzed. Only two sets of materials, $E/\sigma_0 = 800$ and 300 with $n = 5$ and 20 in Table 2 are considered here. The variations of A_2 along the crack front are illustrated in Fig. 7. Compared to Fig. 6, the constraint level of the CR(B) and SE(B) specimens in terms of A_2 are slightly decreased. Similarly, the material with $E/\sigma_0 = 800$ exhibits a more distinct biaxial effect than the other material. The normalized J values at each front location for the specimens are also examined, as shown in Fig. 9. The position of the maximum J is shifted from the midplane of the SE(B) specimen toward the outside surface, with an increase in the local J by only 5%. The distributions of J for the CR(B) specimens follow those shown in Fig. 8.

The results from the above analysis are consistent with several experimental investigations. Hohe et al. [3] carried out experiments on the CR(B) and the SE(B) specimens of 22NiCrMo37 steel at two different temperatures in the ductile-to-brittle transition (DBT) region. At the lower test temperature, the fracture toughness distribution of the CR(B) specimens with a shallow crack $a_0/W \approx 0.08$ is almost identical to that of the SE(B) specimens with a slightly deeper crack ($a_0/W \approx 0.13$). At the higher test temperature, the failure probability of the CR(B) specimens with $a_0/W \approx 0.08$ is significantly higher than that of their SE(B) counterparts with $a_0/W \approx 0.13$. Since the fracture toughness distribution in the DBT region can be characterized by master curve approach, the extent of biaxial effect is quantified in terms of a shift in master curve reference temperature T_0 determined by the subsets of the fracture toughness data for each specimen type at two temperatures. The difference in the reference temperature T_0 between the CR(B) specimens and the SE(B) specimens increased from $-0.2\,^{\circ}\mathrm{C}$ at the lower test temperature to $+23.9\,^{\circ}\mathrm{C}$ at the higher test temperature, showing that the biaxial loading effect on fracture toughness is gradually enhanced by increasing temperatures. Note that for the same material, the yield stress is lower at higher temperature compared that at lower temperatures. This experimental observation by Hohe et al. [3] is reflected by our numerical results in Figs. 6(*a*) and 7(*a*) where material with lower yield stress ($E/\sigma_0 = 800$) shows more biaxial effect in terms of A_2.

Similar trend on the biaxial loading effect on fracture toughness in the DBT region is found in Bass et al. [1]. Bass et al. [1] tested the CR(B) specimens with various biaxial ratio, namely 0:1, 0.6:1, and 1:1, at $-30\,^{\circ}\mathrm{C}$ and $-5\,^{\circ}\mathrm{C}$. It was reported that little biaxial effect was observed in terms of K_{Jc} data for the three biaxial ratios at $-30\,^{\circ}\mathrm{C}$, whereas the test data demonstrated a significant effect of biaxial loading at $-5\,^{\circ}\mathrm{C}$. At this higher test temperature, the mean value of biaxial (1:1) fracture toughness is only 58% of the mean fracture toughness from uniaxial tests.

It may be concluded from our numerical analysis and these experimental observations that the effect of biaxial loading on cleavage fracture toughness for the CR(B) specimen may

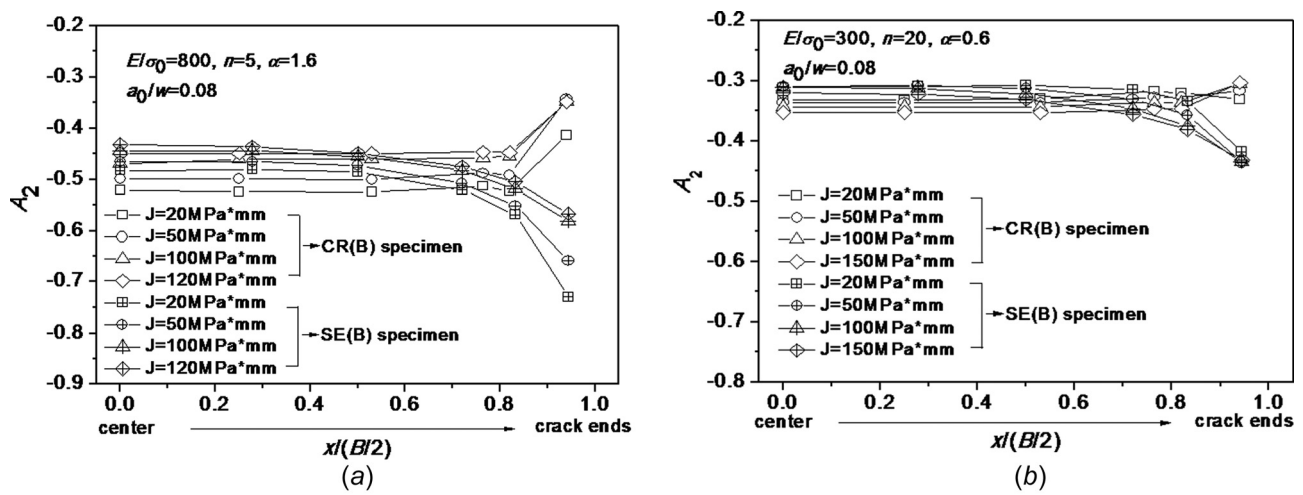

Fig. 7 Variation of A_2 across the thickness with crack depth $a_0/W = 0.08$ for: (*a*) material 1 ($E/\sigma_0 = 800$, $n = 5$, $\alpha = 1.6$) and (*b*) material 3 ($E/\sigma_0 = 300$, $n = 20$, $\alpha = 0.6$)

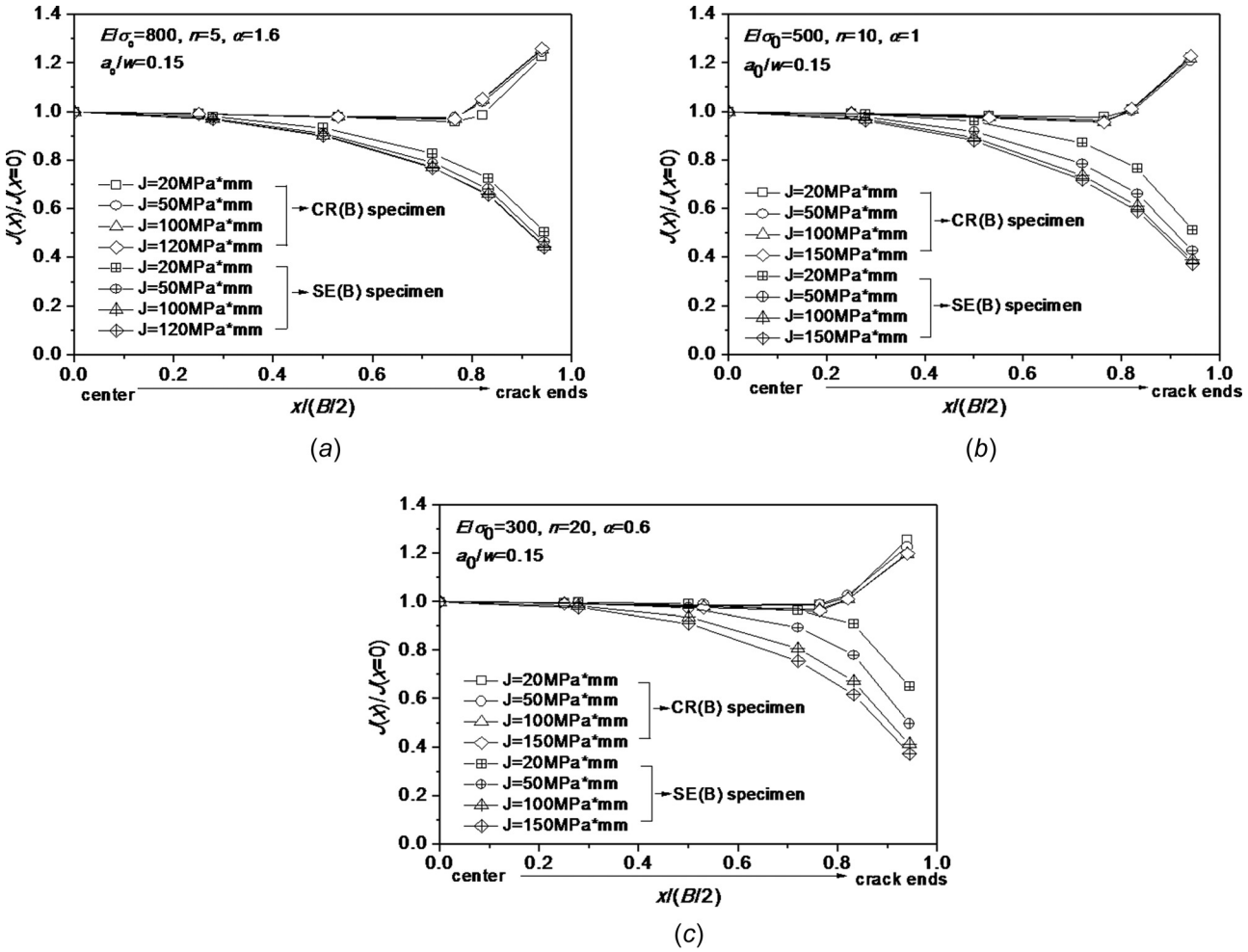

Fig. 8 Variation of J across the thickness with crack depth $a_0/W = 0.15$ for: (*a*) material 1 ($E/\sigma_0 = 800$, $n = 5$, $\alpha = 1.6$), (*b*) material 2 ($E/\sigma_0 = 500$, $n = 10$, $\alpha = 1$), and (*c*) material 3 ($E/\sigma_0 = 300$, $n = 20$, $\alpha = 0.6$)

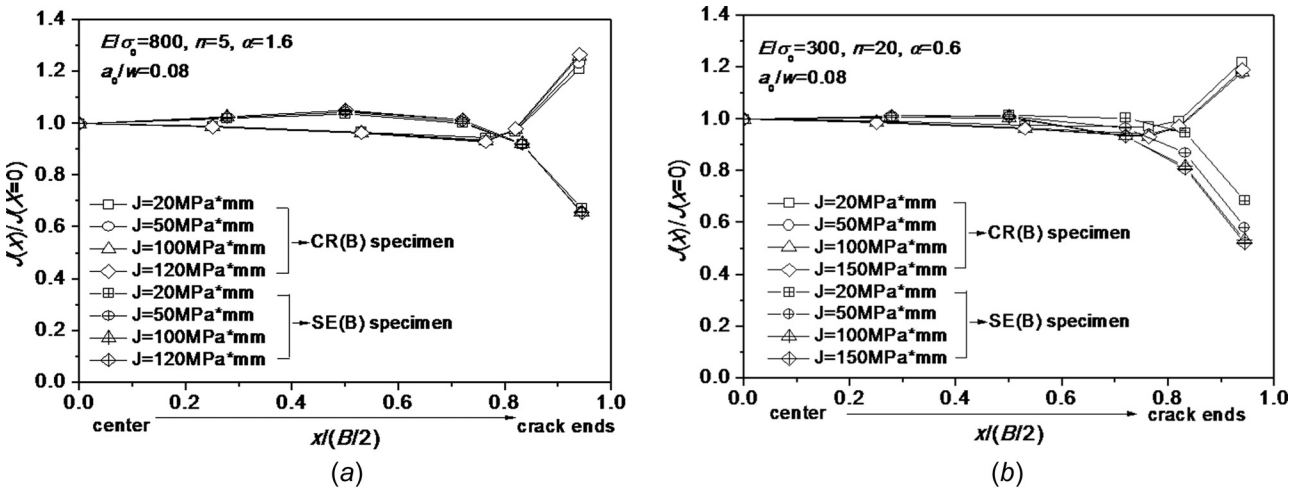

Fig. 9 Variation of J across the thickness with crack depth $a_0/W = 0.08$ for: (*a*) material 1 ($E/\sigma_0 = 800$, $n = 5$, $\alpha = 1.6$), (*b*) material 3 ($E/\sigma_0 = 300$, $n = 20$, $\alpha = 0.6$)

gradually become pronounced with the increase of test temperature due to the variations in material tensile properties. Additionally, the shallow crack-induced constraint loss can be partially inhibited by the biaxial loading at a higher temperature, whereas at a lower temperature, shallow cracks have a more significant effect on fracture toughness than does biaxial loading.

Conclusions

To investigate the constraint effect under uniaxial and biaxial loading conditions, detailed FE analysis for the CR(B) and SE(B) specimens with crack depths of $a_0/W = 0.08$ and 0.15 combined with the consideration of different material tensile properties are

carried out. The variations of constraint with crack depths and material properties are quantified in terms of the A_2 parameter. The results can be summarized as follows:

(1) The constraint effect under biaxial loading is dependent on the tensile properties of the materials. A more pronounced biaxial effect is shown in the specimen with lower yield stress. This indicates that the biaxial effect on material fracture toughness may be more obvious at higher temperatures in the DBT region since the yield stress decreases with increasing temperature. Consequently, in RPV structural integrity assessment, more attention may be given to the biaxial loading effect at a relatively higher temperature during a thermal–mechanical transient (e.g., a pressurized thermal shock event). In addition, when assessing the irradiation-induced fracture toughness degradation, materials exposed to low neutron fluence irradiation has lower yield stress compared to the highly irradiated condition and therefore may show greater effect due to biaxial loading.
(2) For the crack depths studied, there is no obvious constraint difference due to the biaxial loading.
(3) As a final note, the effect of the material properties on the biaxial constraint revealed in this study is resulted from a combination of the yield stress and the strain-hardening exponent. It would be interesting to further evaluate the influence of the yield stress and the strain-hardening exponent separately.

Acknowledgment

Yupeng Cao and Yinbiao He are grateful for the support of the Major Program of Large-Scale Advanced PWR and HTGR Nuclear Power Plant of China (2014ZX06002001). Guian Qian and Markus Niffenegger are thankful for the financial support of the PROBAB Project provided by the Swiss Federal Nuclear Safety Inspectorate (ENSI) (DIS-VertragNr. H-100668).

Nomenclature

a_0 = initial crack depth
A_2 = constraint parameter in the J–A_2 theory
B = specimen thickness or crack front lengths
E = elastic modulus
I_n = an integration constant
J = J-integral
J_c = critical J-integral
K_c = material fracture toughness
L = a characteristic length parameter
n = hardening exponent in the Ramberg–Osgood stress–strain relationship
s_1, s_2, s_3 = stress power exponents in the J–A_2 theory
S_1, S_2 = span widths on the longitudinal and the transverse beam arms
T_0 = master curve reference temperature
W = specimen width
α = parameter in the Ramberg–Osgood stress–strain relationship
ε_0 = strain parameter in the Ramberg–Osgood stress–strain relationship
ν = Poisson's ratio
$\tilde{\sigma}_{ij}^{(k)}(\theta, n)$ = dimensionless stress functions in the J–A_2 theory
σ_0 = yield stress

References

[1] Bass, B. R., McAfee, W. J., Williams, P. T., and Pennell, W. E., 1999, "Fracture Assessment of Shallow-Flaw Cruciform Beams Tested Under Uniaxial and Biaxial Loading Conditions," Nucl. Eng. Des., **188**(3), pp. 259–288.
[2] Joyce, J., Link, R., and Gaies, J., 2005, "Evaluation of the Effect of Biaxial Loading on the Reference Temperature Using a Cruciform Specimen Geometry," J. ASTM Int., **2**(1), pp. 1–18.
[3] Hohe, J., Luckow, S., Hardenacke, V., Sguaizer, Y., and Siegele, D., 2011, "Enhanced Fracture Assessment Under Biaxial External Loads Using Small Scale Cruciform Bending Specimens," Eng. Fract. Mech., **78**(9), pp. 1876–1894.
[4] Link, R. E., Joyce, J. A., and Roe, C., 2007, "An Experimental Investigation of the Effect of Biaxial Loading on the Master Curve Transition Temperature in RPV Steels," Eng. Fract. Mech., **74**(17), pp. 2824–2843.
[5] Sharpe, L. W., and Chao, Y. J., 2012, "Quantifying the Constraint of Three-Dimensional Biaxially Loaded Specimens Containing Semi-Elliptical Cracks Using the J-A2 Method," ASME Paper No. PVP2012-78404.
[6] Sharpe, L. W., and Chao, Y. J., 2013, "Constraint Effect in Fracture: Investigation of Cruciform Specimens Using the J-A_2 Method," 13th International Conference on Fracture, Beijing, China, June 16–21, Paper No. S32-034.
[7] Hutchinson, J. W., 1968, "Singular Behaviour at the End of a Tensile Crack in a Hardening Material," J. Mech. Phys. Solids, **16**(1), pp. 13–31.
[8] Hutchinson, J. W., 1968, "Plastic Stress and Strain Fields at a Crack Tip," J. Mech. Phys. Solids, **16**(5), pp. 337–342.
[9] Rice, J. R., and Rosengren, G. F., 1968, "Plane Strain Deformation Near a Crack Tip in a Power-Law Hardening Material," J. Mech. Phys. Solids, **16**(1), pp. 1–12.
[10] ASTM, 2016, "Standard Test Method for Determination of Reference Temperature, to, for Ferritic Steels in the Transition Range," ASTM International, West Conshohocken, PA, Standard No. ASTM E1921-16.
[11] Yang, S., Chao, Y. J., and Sutton, M. A., 1993, "Complete Theoretical Analysis for Higher Order Asymptotic Terms and the HRR Zone at a Crack Tip for Mode I and Mode II Loading of a Hardening Material," Acta Mech., **98**(1–4), pp. 79–98.
[12] Yang, S., Chao, Y. J., and Sutton, M. A., 1993, "Higher Order Asymptotic Crack Tip Fields in a Power-Law Hardening Material," Eng. Fract. Mech., **45**(1), pp. 1–20.
[13] Chao, Y. J., Yang, S., and Sutton, M. A., 1994, "On the Fracture of Solids Characterized by One or Two Parameters: Theory and Practice," J. Mech. Phys. Solids, **42**(4), pp. 629–647.
[14] Chao, Y. J., and Zhang, L., 1997, "Tables of Plane Strain Crack Tip Fields: HRR and Higher Order Terms," Department of Mechanical Engineering, University of South Carolina, Columbia, SC, Report No. ME-Report97-1.
[15] Wang, Z. X., Zhang, R. F., Chao, Y. J., and Lam, P. S., 2011, "Elastic-Plastic Constraint Analysis of Semi-Elliptic Surface Cracks in X100 Pipeline Steel," ASME Paper No. PVP2011-57715.
[16] ABAQUS/Standard, 2011, "ABAQUS/Standard," Dassault Systèmes Simulia Corp., Vélizy-Villacoublay, France.